biomolecules

MDPI

Article

Nudifloramide Accumulation Is Associated with Myocardial Hypertrophy and MEK/ERK Activation in Cardiorenal Syndrome Type 4

Minlong Wei [1,†], Yajun Lei [1,†], Jialu Wen [1], Jingyan Feng [1], Xiao Dong [1], Cuiping Jiang [2], Fenghua Zhou [2,*] and Menghua Liu [1,*]

[1] Key Laboratory of Drug Metabolism Research and Evaluation of the State Drug Administration, Guangdong Provincial Key Laboratory of New Drug Screening, School of Pharmaceutical Sciences, Southern Medical University, Guangzhou 510515, China; weimlong3@mail.sysu.edu.cn (M.W.); leiyajun55@gmail.com (Y.L.); wenjialu669@gmail.com (J.W.); jingyf128@gmail.com (J.F.); wuf110635@gmail.com (X.D.)

[2] School of Traditional Chinese Medicine, Southern Medical University, Guangzhou 510515, China; jxiaqing126@smu.edu.cn

* Correspondence: wendy515@smu.edu.cn (F.Z.); liumenghua@smu.edu.cn (M.L.)

† These authors contributed equally to this work.

Abstract

Cardiorenal syndrome type 4 (CRS-4) is a major cause of mortality in chronic kidney disease (CKD). The uremic toxin nudifloramide (2PY) is reported as a potential factor independently associated with cardiovascular risk in CKD, but its potential myocardial effects and mechanisms remain unknown. Here, we established a CRS-4 rat model via 5/6 Nx. Plasma untargeted metabolomics and cardiac transcriptomics were integrated with the EUTox database to screen cardiotoxic uremic toxins, and network toxicology was used to predict mechanisms. In vivo rat experiments and in vitro H9c2 cardiomyocyte models were used for further validation. As a result, CRS-4 rats developed renal failure, myocardial hypertrophy, and systolic dysfunction, accompanied by marked metabolic and transcriptional remodeling. Cross-referencing with the EUTox database identified 2PY as a candidate cardiotoxic uremic toxin. Chronic 2PY exposure in rats decreased LVEF, LVFS, and cardiac output; increased cardiomyocyte cross-sectional area; and upregulated plasma NT-proBNP and NT-proANP. Molecular docking and molecular dynamics simulations predicted PRKCE as a candidate interacting protein of 2PY, suggesting a potential upstream mechanism for MEK/ERK activation. Western blot and qPCR assays confirmed that 2PY significantly activated the MEK/ERK signaling pathway both in vivo and in vitro. Furthermore, the MEK inhibitor U0126 effectively blocked 2PY-triggered MEK/ERK phosphorylation and largely reversed 2PY-induced cardiomyocyte hypertrophy. Collectively, these findings indicate that increased 2PY abundance is associated with myocardial hypertrophy and MEK/ERK activation, providing a mechanistic basis for cardiovascular risk assessment and targeted intervention in CKD.

Keywords: cardiorenal syndrome type 4; nudifloramide; myocardial hypertrophy; MEK/ERK pathway; network toxicology

Check for updates

Academic Editor: Utpal Sen

Received: 5 October 2026
Revised: 25 November 2026
Accepted: 26 November 2026
Published: 28 November 2026

Copyright: © 2026 by the authors. Licensee MDPI, Basel, Switzerland. This article is an open access article distributed under the terms and conditions of the Creative Commons Attribution (CC BY) license.

1. Introduction

Cardiorenal syndrome type 4 (CRS-4, also known as chronic renocardiac syndrome) is a complex clinical syndrome characterized by secondary cardiac structural and functional

abnormalities that arise from progressive chronic kidney disease (CKD) [1]. According to the 2023 Global Burden of Disease study, CKD affects approximately 788 million adults worldwide and ranks as the ninth leading cause of death globally [2]. Cardiovascular disease is among the most frequent and lethal complications of CKD, accounting for approximately 31.2% of all-cause mortality in this patient population [3,4]. Left ventricular hypertrophy (LVH) with myocardial fibrosis is the hallmark of uremic cardiomyopathy, affects most patients with advanced CKD, and serves as a strong independent predictor of cardiovascular mortality [5,6]. Current clinical management of CRS-4 primarily aims to slow CKD progression and control volume overload, with standard regimens including diuretics, renin–angiotensin–aldosterone system (RAAS) inhibitors, and sodium–glucose cotransporter 2 (SGLT2) inhibitors [7,8]. However, these interventions remain largely symptomatic and show limited efficacy in improving long-term outcomes. Furthermore, such therapies may also induce electrolyte disturbances or worsen advanced cardiorenal deterioration [8]. Therefore, elucidating the core pathogenic drivers and identifying novel molecular targets of CRS-4 from a mechanistic perspective are critically needed.

Emerging evidence has revealed that the abnormal accumulation of uremic toxins serves as a critical intermediate link between renal failure and secondary myocardial injury [9], acting in concert with and aggravating hemodynamic disorders, microinflammation, and oxidative stress [10]. As the glomerular filtration rate (GFR) declines, uremic toxins accumulate in the circulation and injure the myocardium through mechanisms including mitochondrial dysfunction, inflammatory cascade activation, and oxidative stress, thereby driving cardiomyocyte apoptosis and remodeling [11–13]. Although renal replacement therapies such as hemodialysis are widely used in clinical practice, their efficacy in clearing many of these toxins is intrinsically limited [14]. Clinical data indicate that dialysis alone fails to effectively prevent adverse cardiovascular outcomes in CRS-4 patients [15,16].

To date, research on the cardiovascular toxicity of uremic toxins has primarily focused on protein-bound uremic toxins (PBUTs; e.g., indoxyl sulfate [17], *p*-cresol sulfate [18]) and middle-to-large molecular toxins (e.g., fibroblast growth factor-23 [19]). Recent studies have demonstrated that certain small-molecule uremic toxins, including trimethylamine *N*-oxide [20] and asymmetric dimethylarginine [21], are capable of inducing cardiovascular injury upon chronic accumulation. Nudifloramide (1-methyl-6-oxopyridine-3-carboxamide, 2PY) is a representative small-molecule uremic toxin. With CKD progression, 2PY markedly accumulates in patient blood, reaching circulating concentrations approximately 5–6-fold higher than those in healthy controls [22,23]. Clinical cohort analyses have demonstrated that elevated circulating 2PY is significantly associated with an increased risk of major adverse cardiovascular events [24]. However, direct experimental evidence for its cardiotoxicity, particularly myocardial hypertrophy, remains scarce.

Therefore, this study established a 5/6 nephrectomy-induced CRS-4 rat model. By integrating plasma metabolomics and cardiac transcriptomic screening with systematic in vivo and in vitro validation, we aimed to elucidate the detailed mechanisms underlying 2PY-mediated myocardial hypertrophy. Here, we demonstrate that 2PY exposure was associated with myocardial hypertrophy and increased MEK/ERK signaling activity. and that the MEK inhibitor U0126 rescues this phenotype. In silico analyses further implicate protein kinase C epsilon (PRKCE) as a potential direct target of 2PY that may mediate RAS/MEK/ERK activation. These results may refine cardiovascular risk assessment in CKD patients and identify candidate targets against CRS-4.

2. Materials and Methods

2.1. Reagents

Isoflurane for animal anesthesia was purchased from RWD Life Science Co., Ltd. (Shenzhen, China). Creatinine (Cr) and blood urea nitrogen (BUN) assay kits were obtained from Nanjing Jiancheng Bioengineering Institute (Nanjing, China). Enzyme-linked immunosorbent assay (ELISA) kits for B-type natriuretic peptide (BNP), N-terminal pro-B-type natriuretic peptide (NT-proBNP), and N-terminal pro-atrial natriuretic peptide (NT-proANP) were purchased from Wuhan Fine Biotech Co., Ltd. (Wuhan, China). Primary antibodies against MEK1, phospho-MEK1, ERK1/2, and phospho-ERK1/2 were obtained from HUABIO (Hangzhou, China), while anti-RAF1 and anti-GAPDH antibodies were purchased from Proteintech (Wuhan, China) and ImmunoWay Biotechnology (Plano, TX, USA), respectively. High-glucose Dulbecco's modified Eagle medium (DMEM) and fetal bovine serum (FBS) were obtained from Gibco (Carlsbad, CA, USA) and ExCell Bio (Suzhou, China), respectively. Tris-buffered saline with Tween-20 (TBST) was obtained from Labgic Technology Co., Ltd. (Beijing, China). The 2PY reference standard and the MEK inhibitor U0126 were purchased from MedChemExpress (MCE, Monmouth Junction, NJ, USA).

2.2. Experimental Animals

Healthy male Sprague-Dawley (SD) rats initially weighing 250–280 g were obtained from Southern Medical University (Guangzhou, China). Animals were housed at 22 ± 2 °C, 50–60% humidity, 12 h light/dark, with free access to food and water, and acclimatised for 1 week before experiments. All animal procedures were performed in strict accordance with the guidelines for ethical conduct in the care and use of experimental animals. The experimental protocol was approved by the Animal Ethics Committee of Southern Medical University (Ethical Approval: No. SMUL202411005, Approval Date: 9 December 2024).

A rat model of CRS-4 was established using a two-step 5/6 Nx procedure [25]. Twelve male SD rats were randomly assigned to the sham-operated (Sham) group or the 5/6 Nx (Model) group, and all surgeries were performed under isoflurane inhalation anesthesia using sterile techniques. In the first surgery, the left kidney of Model rats was exposed, and the upper and lower poles were resected, leaving approximately one-third of the renal parenchyma intact. After a 1-week recovery, the right renal pedicle was ligated and the right kidney was completely excised. Sham rats underwent identical bilateral kidney exposure at both stages without tissue resection. Postoperatively, rats received aspirin (25 mg/kg/day) and penicillin (4×10^4 U/kg/day) for 3 consecutive days to provide analgesia and infection prophylaxis. Body weight was measured weekly. At 8 weeks post-5/6 Nx, cardiac structure and function were assessed using a small animal ultrasound system (Vevo 2100, Fujifilm VisualSonics, Toronto, ON, Canada). Transthoracic echocardiography was performed under isoflurane anesthesia (induced at 4% and maintained at 1.5–2% in 100% oxygen). Left ventricular internal diameter at end-diastole (LVIDd) and end-systole (LVIDs) were measured, and left ventricular ejection fraction (LVEF), left ventricular fractional shortening (LVFS), and cardiac output (CO) were calculated by the system software. All measurements were performed by an operator blinded to group allocation, and values were averaged over three consecutive cardiac cycles. The same echocardiographic protocol was used at 5 weeks after 2PY intervention. Plasma was then collected via retro-orbital venous plexus sampling for untargeted metabolomics analysis and for measurement of creatinine (Cr), blood urea nitrogen (BUN), and plasma B-type natriuretic peptide (BNP) using commercial assay kits.

For the in vivo 2PY intervention, another twelve male SD rats were randomly allocated into the Control group and the 2PY group. 2PY was dissolved in sterile drinking water at a concentration of 0.135% (*w*/*v*, 1.35 mg/mL), and rats in the 2PY group received this

medicated water ad libitum for 5 consecutive weeks. This concentration was calculated assuming a rat body weight of 300 g and daily water intake of 33.3 mL, yielding an estimated target dose of 150 mg/kg/day (~45 mg 2PY per rat daily). Rats were housed three per cage with 100 mL drug-containing water provided daily. Control rats received standard sterile drinking water. At 5 weeks post-intervention, cardiac structure and function were evaluated using the Vevo 2100 ultrasound system, and plasma NT-proBNP and NT-proANP levels were measured using commercial assay kits. At the end of each experiment, all rats were euthanized by isoflurane overdose. The heart was removed and weighed, and the cardiac index was calculated as the ratio of heart weight to body weight (mg/g). Kidney and heart tissues (CRS-4 model) or heart tissues (2PY intervention) were sectioned longitudinally along the midline. One half was immediately fixed in 4% paraformaldehyde for histological analysis, and the other half was stored at −80 °C for molecular experiments. Liver tissues from CRS-4 model and Sham rats were also collected and stored at −80 °C for subsequent molecular analyses.

2.3. Hematoxylin–Eosin (H&E) Staining

Kidney and heart tissues were fixed in 4% paraformaldehyde for more than 24 h, dehydrated through graded ethanol, cleared in xylene, and paraffin-embedded. Tissue sections (4–5 μm) were deparaffinized, rehydrated, and stained with H&E following standard protocols [26]. Stained slides were dehydrated, cleared, and mounted with neutral balsam for light microscopy. Histopathological evaluation was performed independently by two investigators in a blinded manner. For kidney tissues, ImageJ (v1.54g) software (NIH, Bethesda, MD, USA) was used to quantify the renal injury area ratio, which was calculated as the percentage of injured area relative to the total renal tissue area. For morphological quantification, we analyzed 5 random non-overlapping fields per animal (20 fields in total from 4 animals per group), measuring an average of 100 cardiomyocytes per animal. Data were averaged per animal, with the animal serving as the statistical unit.

2.4. Masson's Trichrome Stain

Collagen deposition and fibrosis in kidney and heart tissues were assessed by Masson's trichrome staining following standard protocols [26]. Histological images were acquired under standardized conditions using light microscopy. Quantitative analysis was performed independently by two investigators in a blinded manner. Five random non-overlapping fields per section were captured at 200× magnification, and the collagen-positive (blue-stained) area was quantified using Image-Pro Plus 6.0 software (Media Cybernetics, Silver Spring, MD, USA). Fibrosis was expressed as the percentage of positive-stained area relative to the total field area.

2.5. Wheat Germ Agglutinin (WGA) Staining

WGA staining was used to assess cardiomyocyte cross-sectional area (CSA) in the 2PY intervention study. Paraffin-embedded heart sections (4–5 μm) were stained with 5 μg/mL fluorophore-conjugated WGA in the dark at room temperature for 30 min, counterstained with DAPI, and mounted with an anti-fade medium. Images were acquired under a confocal microscope [27]. CSA was quantified using ImageJ (v1.54g) software (NIH, Bethesda, MD, USA) by two independent investigators in a blinded manner. At least 50 intact cardiomyocytes from at least 5 random fields per section were manually traced along WGA-stained cell membranes. Results were expressed as mean CSA (μm^2) to evaluate cardiomyocyte hypertrophy.

2.6. Untargeted Plasma Metabolomics

Plasma samples (100 µL) were mixed with 400 µL of pre-cooled methanol/acetonitrile (1:1, *v*/*v*) for protein precipitation. After vortexing and centrifugation (14,000× *g*, 4 °C, 20 min), supernatants were vacuum-dried, redissolved in 100 µL acetonitrile/water, and re-centrifuged under identical conditions to acquire clarified supernatants for analysis. Metabolomic profiling was performed on a Vanquish UHPLC coupled to an Orbitrap Exploris 480 high-resolution mass spectrometer (Thermo Fisher Scientific, Waltham, MA, USA). A HILIC column was used for chromatographic separation with 25 mM ammonium acetate-ammonia aqueous solution (mobile phase A) and pure acetonitrile (mobile phase B) at 0.5 mL/min (detailed gradients in Table S1). Full-scan MS acquisition was conducted in dual ESI positive/negative modes (*m*/*z* 70–1200) with spray voltages of 3.5 kV and 2.8 kV, respectively. Samples were injected in random order. Pooled quality control (QC) samples, prepared by combining equal aliquots of all plasma samples, were injected intermittently to monitor instrument stability. Blank samples were included to filter contaminants. During data preprocessing, signal drift correction and feature filtering were performed based on strict variability thresholds (RSD > 50% and missing values > 50% were excluded). Raw MS data were converted to mzXML using ProteoWizard and processed in XCMS for peak extraction (mass tolerance < 10 ppm), alignment and grouping, with CAMERA-based adduct annotation. Metabolite annotation was performed against an in-house database established by Shanghai Applied Protein Technology. Annotation relied on combined matching of retention time, accurate mass (mass error < 10 ppm), MS/MS fragmentation patterns and collision energy, followed by rigorous manual curation; annotated metabolites meet an identification confidence of Level 2 or above. After filtering missing values (>50% presence) and total area normalization, differential metabolites were determined by multivariate analysis (R/ropls) and Student's *t*-test (VIP > 1, $p < 0.05$). The robustness of each OPLS-DA model was evaluated by reporting R^2 and Q^2 values together with permutation test results to assess the potential risk of overfitting. Metabolomic analysis was performed by Shanghai Applied Protein Technology (Shanghai, China) [28].

2.7. Cardiac Tissue Transcriptomics

RNA-seq was performed by Shanghai Applied Protein Technology Co., Ltd. (Shanghai, China). Briefly, total RNA was extracted from heart tissue with TRIzol reagent. RNA purity and integrity were evaluated using a NanoDrop ND-2000 spectrophotometer (Thermo Fisher Scientific, Waltham, MA, USA) and Agilent Bioanalyzer 4150 system (Agilent Technologies, Santa Clara, CA, USA), respectively. Only samples with RNA integrity number (RIN) > 8 were used for library preparation. RNA libraries were constructed from 1 µg total RNA using the ABclonal mRNA-seq Kit (ABclonal, Woburn, MA, USA) and sequenced on an Illumina NovaSeq 6000 platform (Illumina, San Diego, CA, USA). Each sample yielded 5.74–10.78 Gb of data (average 53 million clean reads). Clean reads were aligned to the Rattus norvegicus reference genome (Ensembl May 2021) using HISAT2. The total mapping rate was 93.91%–97.81% (unique: 78.53%–87.12%). High data reliability was confirmed by Q30 > 93.9%, error rate 0.02%, and inter-sample correlation > 0.97. Gene-level read counts were computed by FeatureCounts. Differentially expressed genes (DEGs) were identified using DESeq2 based on the raw count matrix ($|\log_2(\text{fold change})| > 1$, *padj* < 0.05). FPKM values were calculated for data visualization purposes. Functional enrichment of DEGs for Gene Ontology (GO) and KEGG pathways was implemented in clusterProfiler (v4.20), with $p < 0.05$ considered statistically significant [29].

2.8. Network Toxicology

To systematically identify key molecular targets mediating uremic-toxin-induced cardiac injury in CRS-4, a network toxicology approach integrating plasma metabolomic profiling, cardiac transcriptomic sequencing, and disease-gene database mining was applied. Based on differential metabolites identified via plasma metabolomics, abnormally accumulated uremic toxins under CRS-4 conditions were screened by cross-referencing the European Uremic Toxin Work Group (EUTox) database. Canonical SMILES strings of candidate uremic toxins were retrieved from the PubChem database (https://pubchem.ncbi.nlm.nih.gov/; accessed on 14 May 2026). Disease-related targets were first collected from GeneCards (http://www.genecards.org; accessed on 16 May 2026), CTD (https://ctdbase.org; accessed on 16 May 2026), and OMIM (http://www.omim.org; accessed on 16 May 2026) databases using the search terms "Cardiac hypertrophy", "Heart failure", and "Cardiorenal syndrome type 4". The obtained disease-target sets were merged with differentially expressed genes (DEGs) from cardiac transcriptome sequencing, followed by deduplication to construct a comprehensive target dataset for CRS-4-associated cardiac injury. Potential macromolecular targets of uremic toxins were then predicted using four web servers: SwissTargetPrediction (http://www.swisstargetprediction.ch/; accessed on 15 May 2026), TargetNet (http://targetnet.scbdd.com; accessed on 15 May 2026), PharmMapper (http://lilab.ecust.edu.cn/pharmmapper/; accessed on 15 May 2026), and SuperPred (https://prediction.charite.de/index.php; accessed on 15 May 2026). Candidate targets linking uremic toxins to myocardial injury were acquired by intersecting toxin-predicted targets with the comprehensive CRS-4-associated cardiac-injury target dataset. Gene Ontology (GO) and Kyoto Encyclopedia of Genes and Genomes (KEGG) enrichment analyses for overlapping targets were performed via Metascape (https://metascape.org/; accessed on 20 May 2026) to explore the molecular mechanisms underlying uremic-toxin-mediated cardiotoxicity. Intersection targets were submitted to the STRING database (v12, https://cn.string-db.org/; accessed on 20 May 2026) to build a protein–protein interaction (PPI) network. Functional modules within the PPI network were detected using the Leiden algorithm implemented in the R igraph package (v1.4.3, resolution = 1.0). The resulting network was imported into Cytoscape (v3.10.3), and the cytoHubba plugin (v0.7.0) was utilized for topological assessment based on four metrics: MCC, Degree, Betweenness, and Bottleneck. Hub proteins supported by all four topological metrics were selected for subsequent molecular docking analysis.

2.9. Molecular Docking and Molecular Dynamics

The 2PY structure was retrieved from the PubChem database (https://pubchem.ncbi.nlm.nih.gov; accessed on 14 May 2026). Protein structures were obtained from the PDB database (https://www.rcsb.org; accessed on 20 August 2026) and AlphaFold predictions (https://alphafold.ebi.ac.uk; accessed on 20 August 2026). Molecular docking was performed to evaluate the preselected target proteins using Maestro 13.1 (Schrödinger, Inc., New York, NY, USA). The LigPrep module was used to generate ligand conformations, and the Protein Preparation Wizard module was applied for protein structure optimization. The SP mode of the Glide module was adopted to generate optimal protein–ligand complexes and assess receptor–ligand binding affinity. The 2PY structure was docked against the hub proteins identified by the four topological metrics in Section 2.8. The candidate with the lowest GlideScore was selected for subsequent molecular dynamics (MD) simulation. Molecular dynamics (MD) simulations were carried out with GROMACS 2020.6 using the Charmm36 force field. Three independent 100 ns simulations were performed to improve reliability. The topology files of small-molecule ligands were generated via CHARMM-GUI (https://charmm-gui.org; accessed on 21 August 2026). The protein–ligand complex was

solvated in a dodecahedral periodic box using the TIP3P water model, with a minimum distance of 1.0 nm between the protein surface and the box boundary. Na^+ and Cl^- ions were added to neutralize the system charge. Energy minimization was implemented by the steepest-descent algorithm to optimize atomic coordinates and achieve a local potential-energy minimum. NVT and NPT ensemble simulations were conducted to equilibrate the system temperature at 300 K and pressure at 1 bar. After equilibration, production-run MD simulations were performed. Simulation outputs were evaluated by hydrogen-bond analysis, molecular mechanics Poisson–Boltzmann surface area (MM-PBSA) calculations, radius of gyration (Rg), root-mean-square deviation (RMSD), root-mean-square fluctuation (RMSF), and gibbs energy landscape analysis.

2.10. In Vitro Experiment

Rat H9c2 cardiomyocytes were purchased from Guangzhou Cellcook Biotech Co., Ltd. (Guangzhou, China). Cells were cultured in high-glucose DMEM containing 10% FBS and 1% penicillin-streptomycin at 37 °C with 5% CO_2. Log-phase cells were seeded and allowed to adhere for 24 h before interventions. For cell counting kit-8 (CCK-8) viability detection, H9c2 cells (5×10^3 cells/well) were seeded in 96-well plates and treated with gradient 2PY (0–10 mM) for 24 h, with triplicate wells for each condition. Absorbance at 450 nm was measured to calculate relative cell viability, and experiments were repeated at least three times. For formal intervention experiments, H9c2 cells were seeded in 6-well plates (1×10^5 cells/dish). After 24 h of adherence, cells were divided into three groups: control group (standard complete medium), 2PY group (1 mM 2PY-containing medium), and a 2PY + U0126 co-treatment group, in which cells were pre-treated with 10 μM U0126 for 1 h before 1 mM 2PY stimulation. All cells were continuously incubated for 24 h, and cell samples were collected after intervention for subsequent experiments.

Phalloidin staining was conducted to evaluate 2PY-induced cardiomyocyte hypertrophy. In brief, post-intervention cells were routinely washed, fixed, permeabilized, and sequentially stained with fluorescent phalloidin and DAPI. All staining and imaging procedures were conducted under identical conditions. Cell surface area was quantified using ImageJ (v1.54g) software (NIH, Bethesda, MD, USA). The results were expressed as the mean cell area (μm^2) to evaluate 2PY-induced cardiomyocyte hypertrophy.

2.11. Real-Time Quantitative PCR (RT-qPCR)

Total RNA was isolated from rat heart and liver tissues using a Tissue RNA Extraction Kit (Foregene, Chengdu, China). RNA purity was determined using a NanoDrop spectrophotometer, with the A260/A280 ratio maintained between 1.8–2.1. One microgram of qualified total RNA was reverse-transcribed into cDNA in a 20 μL system with PrimeScript RT Master Mix (Takara, Otsu, Japan) (42 °C for 15 min, 95 °C for 30 s). RT-qPCR was carried out on a LightCycler 480 Real-Time PCR System (Roche, Basel, Switzerland) using GoTaq qPCR Master Mix (Promega, Madison, WI, USA) by the SYBR Green method. The 10 μL reaction mixture included 5 μL Master Mix, 3.6 μL ddH_2O, 0.4 μL primer mix (synthesized by Tsingke Biotechnology, Beijing, China; sequences shown in Table S2), and 1 μL cDNA template. Cycling conditions: initial denaturation at 95 °C for 120 s, 40 cycles of 95 °C for 15 s and 60 °C for 60 s. Each sample was run in biological triplicate, and relative mRNA expression was calculated by the $2^{(-\Delta\Delta Ct)}$ method.

2.12. Western Blotting

Total protein was extracted from rat heart tissues and H9c2 cardiomyocytes using pre-cooled RIPA lysis buffer supplemented with protease and phosphatase inhibitor cocktails. Protein concentrations were measured with the BCA Protein Assay Kit (EpiZyme, Shanghai,

China). Equal amounts of protein were mixed with 5× SDS-PAGE loading buffer and heat-denatured. Proteins were separated by SDS-PAGE and electro-transferred onto PVDF membranes under constant current. Membranes were blocked with quick blocking buffer for 1 h at room temperature, and then incubated overnight at 4 °C with primary antibodies: anti-RAF1 (1:1000), anti-ERK1/2 (1:1000), anti-phospho-ERK1/2 (1:1000), anti-MEK1 (1:1000), anti-phospho-MEK1 (1:1000), and anti-GAPDH (1:10,000, loading control). After TBST washing, membranes were incubated with HRP-conjugated secondary antibodies (1:10,000) for 2 h at room temperature. Protein bands were visualized with ECL chemiluminescent substrate and imaged on a Tanon 4800 Automated Chemiluminescent/Fluorescent Imaging System (Tanon, Shanghai, China). Band optical density was quantified using ImageJ (v1.54g) software (NIH, Bethesda, MD, USA) by an analyst blinded to group allocation.

2.13. Statistical Analysis

Data are expressed as the mean ± standard deviation (SD). For comparisons among three or more groups, one-way analysis of variance (ANOVA) followed by an appropriate post hoc test was performed using GraphPad Prism (version 9.0.0). For pairwise comparisons between two groups, the unpaired Student's *t*-test was also performed using GraphPad Prism (version 9.0.0). Weekly body weight data were analyzed by two-way repeated-measures ANOVA or linear mixed-effects model. Non-parametric data, including histological quantitative scores derived from H&E and Masson's trichrome staining, were analyzed using the Mann–Whitney U test. Benjamini–Hochberg false discovery rate correction was applied for plasma metabolomic comparisons and Spearman correlation analyses between the eight metabolites and echocardiographic parameters. Statistical significance was defined as follows: ns (not significant), * $p < 0.05$, ** $p < 0.01$, *** $p < 0.001$, **** $p < 0.0001$. Furthermore, bioinformatic analyses and data visualization for the cardiac transcriptome, plasma metabolome, and network toxicology were conducted using R software. Correlations between plasma metabolite levels and echocardiographic parameters were analyzed using Spearman's rank correlation coefficient, implemented with the function in R (version 4.3.2).

3. Results

3.1. 5/6 Nephrectomy Induces Progressive Renal Failure, Secondary Myocardial Hypertrophy, and Cardiac Systolic Dysfunction in Rats

At 8 weeks post-surgery, the 5/6 Nx rats were systematically evaluated for renal injury and secondary cardiac alterations. Biochemical analysis revealed that plasma Cr and BUN concentrations were markedly elevated in the Model group compared with the Sham group (Figure 1C,D). H&E and Masson's trichrome staining revealed marked renal tissue damage and collagen deposition in the Model group, findings that were further corroborated by semi-quantitative analysis showing significantly higher renal injury area ratio and fibrosis area (Figure 1G,H), validating the successful induction of chronic renal failure.

Secondary cardiac alterations were subsequently evaluated. Despite comparable body weight at week 8 (Figure 1B), the cardiac index and plasma BNP were significantly increased in Model rats (Figure 1E,F), providing initial macroscopic evidence of myocardial hypertrophy. Myocardial morphology showed disordered fiber alignment and enlarged cardiomyocyte cross-sectional area in the Model group, accompanied by marked collagen deposition in the interstitial and perivascular regions and an elevated fibrosis ratio (Figure 1I,J). Echocardiography revealed significant systolic dysfunction in Model rats, with significant reductions in LVEF, LVFS, and CO and a significant increase in LVIDs relative to the Sham group (Figure 1K, Table S3). These results demonstrate that chronic renal

injury drives myocardial hypertrophy and systolic dysfunction, confirming the successful establishment of the CRS-4 rat model.

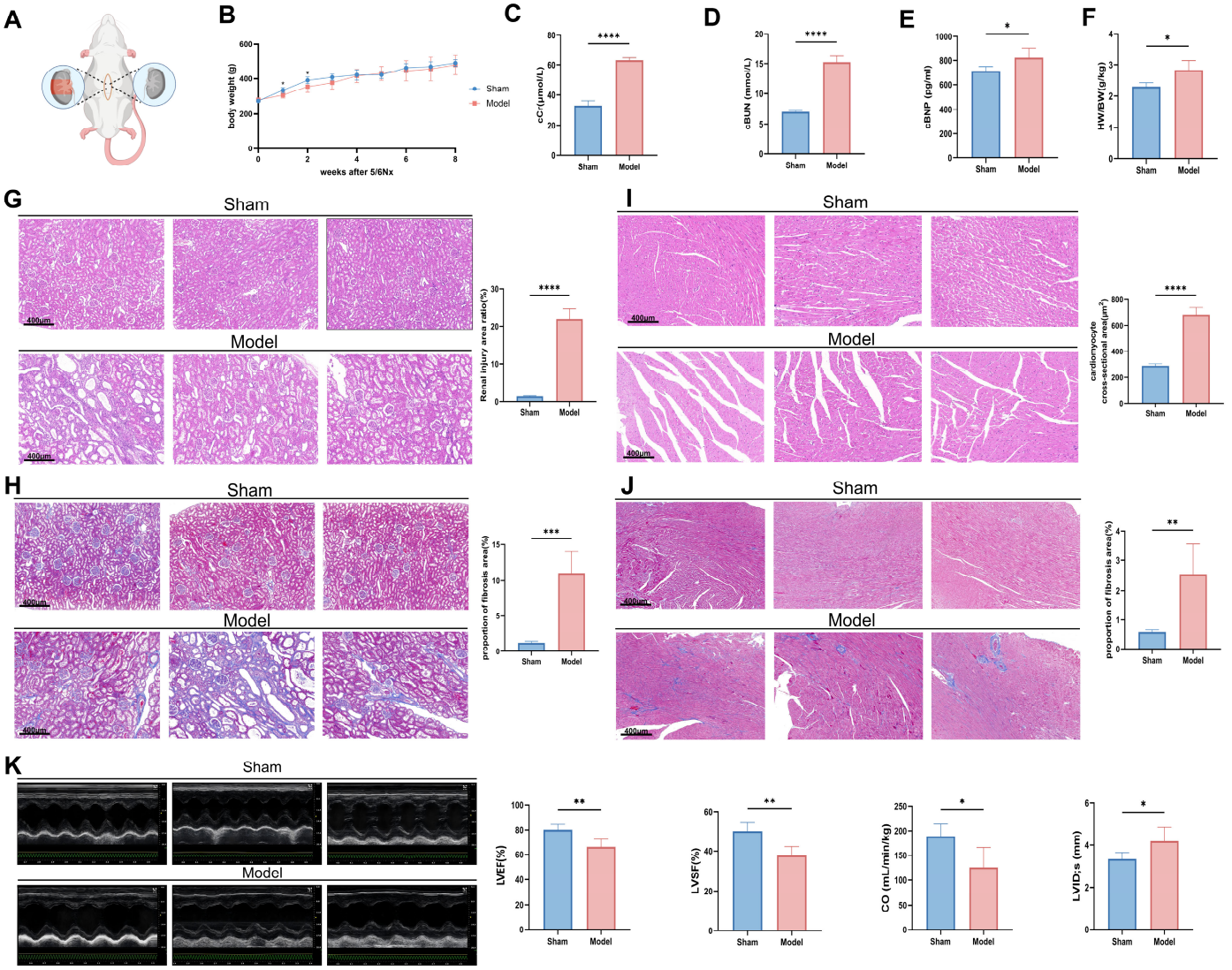

Figure 1. Characterization of the CRS-4 rat model established by 5/6 nephrectomy. (**A**) Schematic diagram illustrating the two-step 5/6 nephrectomy surgical procedure. (**B**) Body weight growth curves of Sham and Model rats within 8 weeks after 5/6 nephrectomy ($n = 6$). (**C**–**F**) Quantitative detection of plasma Cr, BUN, BNP, and heart-to-body weight index (HW/BW) in Sham and Model groups ($n = 4$). (**G**) Representative H&E-stained renal histological images and quantitative analysis of renal injury area ratio. Scale bar, 400 μm ($n = 4$). (**H**) Representative Masson-stained renal sections and quantitative analysis of renal fibrosis area proportion. Scale bar, 400 μm ($n = 4$). (**I**) Representative H&E-stained myocardial tissue sections and quantitative analysis of cardiomyocyte cross-sectional area. Scale bar, 400 μm ($n = 4$). (**J**) Representative Masson-stained myocardial sections and quantitative analysis of myocardial fibrosis area proportion. Scale bar, 400 μm. ($n = 4$) (**K**) Representative M-mode echocardiography images and quantitative analysis of LVEF, LVFS, CO and LVIDs ($n = 5$). Data are presented as mean ± SD. * $p < 0.05$, ** $p < 0.01$, *** $p < 0.001$, **** $p < 0.0001$.

3.2. Plasma Metabolomics Reveals Systemic Metabolite Accumulation and Identifies 2PY as a Candidate Cardiotoxic Uremic Toxin in CRS-4 Rats

Plasma metabolomic profiles differed markedly between the Sham and Model groups. Unsupervised PCA revealed clear distributional separation between the two groups in both ESI^- and ESI^+ modes (Figure 2A,B), which was further confirmed by supervised

OPLS-DA modeling (Figure 2C,D), indicating substantial alterations in plasma metabolic signatures. As shown in the volcano plot, the majority of these metabolites were upregulated in the Model group, among which multiple amino acid derivatives and small-molecule organic acids were the most markedly elevated (Figure 2E), suggesting impaired metabolite clearance. A total of 182 DMs with definitive structural information were identified (Table S4). The *p*-value and m/z distributions of the matched metabolites are shown in Figure 2F. KEGG analysis showed enrichment in pathways including arginine biosynthesis, amino acid biosynthesis, and central carbon metabolism (Figure 2G), suggesting marked disturbances in nitrogen metabolism and energy homeostasis under CRS-4 conditions [30].

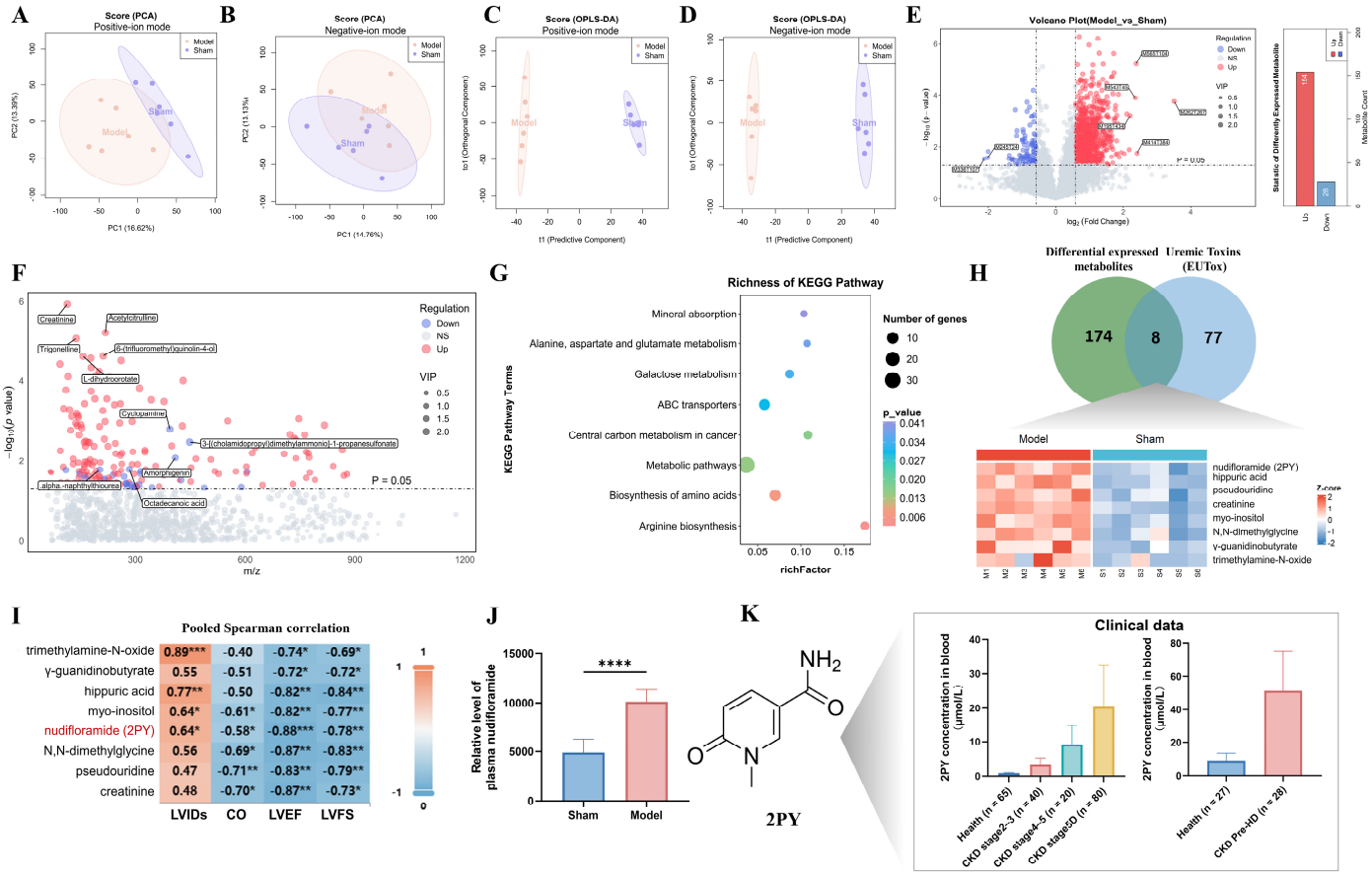

Figure 2. Plasma metabolomic profiling and identification of uremic toxins in CRS-4. (**A**,**B**) PCA score plots displaying the overall metabolic profiles of Sham and Model groups in positive-ion and negative-ion modes ($n = 6$). (**C**,**D**) OPLS-DA score plots showing distinct metabolic separation between Sham and Model groups in positive-ion and negative-ion modes ($n = 6$). (**E**) Volcano plot illustrating differentially expressed metabolites between Model and Sham groups. The right-hand bar graph shows the statistics for up- and down-regulated metabolites. (**F**) Volcano plot showing the distribution of *p* values versus m/z for differential metabolites, annotated with metabolite identities and VIP values. (**G**) Bubble plot for KEGG pathway enrichment analysis of differential metabolites. (**H**) Venn diagram showing the overlap between differential metabolites and EUTox-listed uremic toxins. Heatmap visualizes the expression patterns of eight overlapping uremic toxins. (**I**) Correlation heatmap illustrating Spearman-rank correlations between overlapping uremic toxins and echocardiographic cardiac functional parameters. (**J**) Relative abundance of nudifloramide (2PY) levels in Sham and Model rats determined by untargeted metabolomics ($n = 6$). (**K**) Literature-sourced plasma 2PY concentrations in healthy subjects and patients at different CKD stages ($n = 205$, $n = 55$). Data are presented as mean ± SD. **** $p < 0.0001$.

To screen for uremic toxins with potential cardiotoxic effects, we cross-referenced these differential metabolites against the EUTox database. Eight overlapping molecules were identified, including creatinine, N,N-dimethylglycine, γ-guanidinobutyrate, myo-inositol, 2PY, pseudouridine, trimethylamine-N-oxide (TMAO), and hippuric acid (Figure 2H). In the pooled analysis, 2PY showed the strongest correlation with LVEF ($\rho = -0.88$, $p < 0.001$). However, this association was non-significant in within-group analyses or after adjusting for group and creatinine (Figure 2I and Figure S1). In addition, 2PY was markedly elevated in the plasma of Model rats (Figure 2J) and has been reported to accumulate progressively with CKD progression, reaching 51.27 ± 23.66 μM in uremic patients compared with 9.00 ± 4.47 μM in healthy controls (Figure 2K) [23]. Consequently, despite the confounding effects on its correlation with cardiac function, 2PY was selected as the primary candidate for subsequent investigation. Given that nicotinamide N-methyltransferase (NNMT) and aldehyde oxidase 1 (AOX1) catalyze key steps for 2PY biosynthesis from nicotinamide, we further determined their hepatic mRNA abundance in Model rats. NNMT mRNA was markedly upregulated in liver tissues from Model rats, while AOX1 transcript levels showed no obvious alteration (Figure S1).

3.3. Cardiac Transcriptomics and Network Toxicology Implicate MEK/ERK Signaling in 2PY-Induced Myocardial Injury

RNA-sequencing was performed on cardiac tissues from Model and Sham rats to reveal the transcriptional landscape of CRS-4 cardiomyopathy. PCA and OPLS-DA analyses showed obvious separation between the two groups, indicating substantial transcriptomic reprogramming in the hearts of CRS-4 model rats (Figure 3A,B). Volcano plot analysis identified a total of 377 DEGs between the two groups (Figure 3C). GO enrichment analysis of DEGs revealed alterations in biological process (BP), cellular component (CC), and molecular function (MF; Figure 3D). BP terms were dominated by small-molecule, organic acid, oxoacid, carboxylic acid, lipid, and fatty-acid metabolic processes. CC enrichment pointed to the cell periphery, plasma membrane, extracellular region, and extracellular matrix. MF showed significant enrichment in oxidoreductase activity, active transmembrane transporter activity, C-acyltransferase activity, and medium-chain fatty acid-CoA ligase activity. KEGG pathway analysis showed that DEGs were significantly enriched in metabolic pathways, citrate cycle, oxidative phosphorylation, butanoate metabolism, 2-oxocarboxylic acid metabolism, and carbon metabolism (Figure 3E). These transcriptomic changes indicate severe disturbance of energy metabolism and mitochondrial bioenergetic dysfunction in CRS-4 hearts, providing a pathophysiological basis whereby NAD^+-derived uremic metabolite accumulation may directly impair cardiac function [31]. Notably, 2PY represents one of the end-products of NAD^+ degradation [32]. To predict the potential molecular mechanisms underlying 2PY-induced cardiac injury, network-toxicology analysis was performed. A total of 182 putative 2PY targets were predicted. Merging the 377 cardiac transcriptomic DEGs with cardiovascular-disease-associated genes from public databases generated 1971 non-redundant targets, whose subsequent intersection with the above-mentioned targets yielded 55 overlapping candidate genes (Figure 3F). GO enrichment analysis of these overlapping candidate genes revealed predominant enrichment in regulation of apoptotic process, protein phosphorylation, and cellular response to oxygen-containing compounds, while MF terms were mainly enriched in protein serine/threonine kinase activity (Figure 3G). KEGG analysis further showed significant enrichment of these candidate genes in RAS and MAPK signaling pathways (FDR < 0.05; Figure 3H). Furthermore, Leiden-based modular analysis of the PPI network revealed that genes encoding MEK2 (Map2k2), ERK2 (Mapk1), and their upstream regulator Hras and downstream

effector Rps6ka3 were co-localized in a core functional module (Figure 3I), suggesting that the Ras/MEK/ERK axis may serve as a signaling hub of 2PY-induced cardiotoxicity.

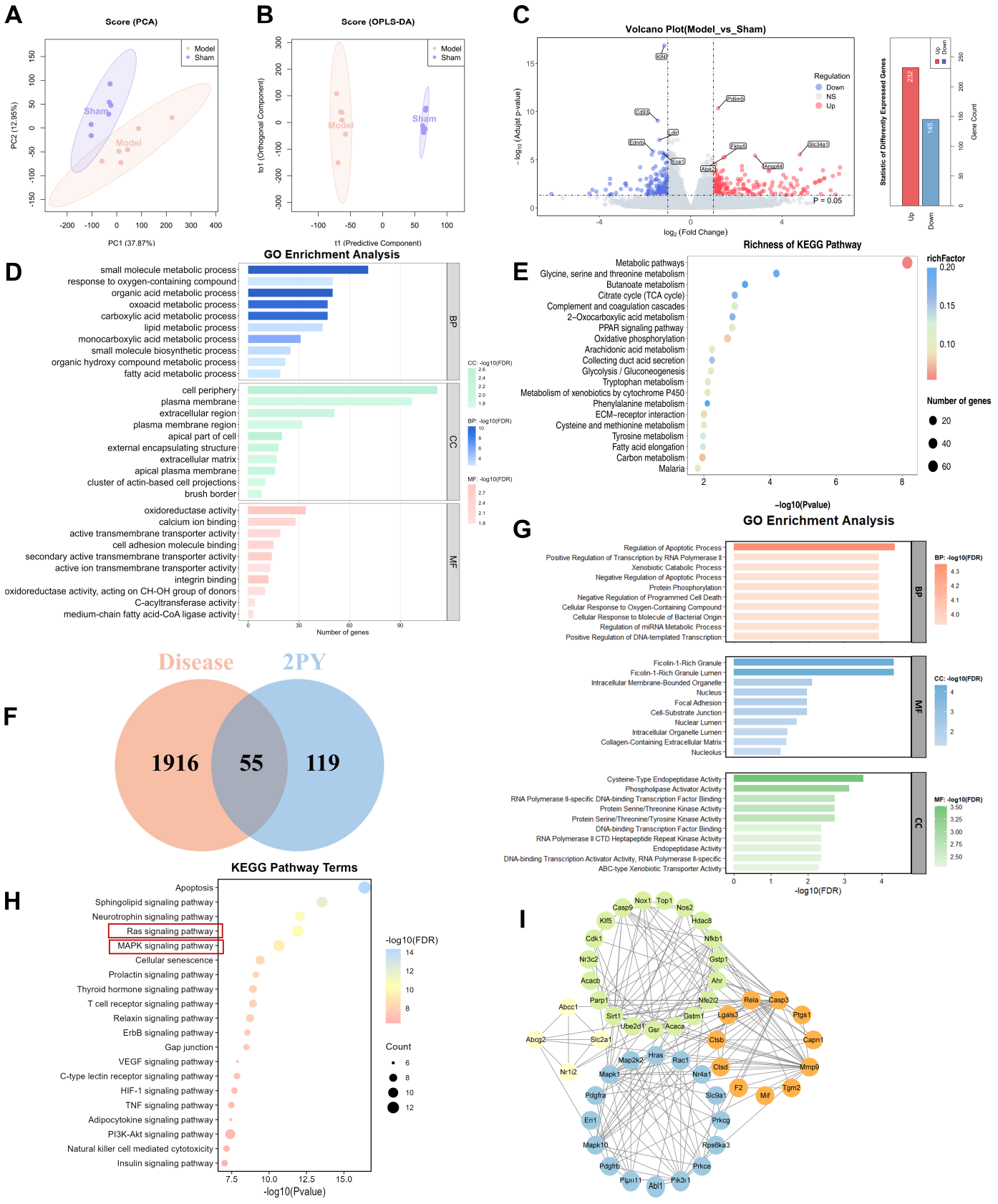

Figure 3. Cardiac transcriptomics and network toxicology reveal the involvement of MEK/ERK signaling in 2PY-triggered myocardial injury. (**A**,**B**) Score plots of PCA and OPLS-DA showing

distinct cardiac transcriptomics between Sham and Model rats ($n = 6$). (**C**) Volcano plot for DEGs in Sham versus Model groups ($n = 6$). (**D**) GO enrichment analysis of DEGs in CRS-4 rats, covering biological process (BP), cellular component (CC), and molecular function (MF). (**E**) Bubble plot of KEGG pathway enrichment for DEGs in CRS-4 rats. (**F**) Venn diagram illustrating the overlap between putative 2PY targets and 1971 non-redundant targets merged from cardiac DEGs and cardiovascular-disease-associated genes from public databases, resulting in 55 overlapping candidate genes. (**G**) GO enrichment analysis of 55 candidate genes. (**H**) KEGG pathway enrichment of 55 candidate genes. The red frame highlights the key RAS and MAPK signaling pathways. (**I**) Leiden-based modular clustering analysis of the PPI network.

3.4. Chronic 2PY Exposure Impairs Cardiac Systolic Function and Induces Myocardial Hypertrophy in Rats

To evaluate the cardiac consequences of chronic 2PY exposure in vivo, rats received 0.135% (w/v) 2PY in drinking water for 5 weeks, followed by echocardiographic assessment (Figure 4A). Compared with the Control group, 2PY-treated rats exhibited markedly reduced LVFS, LVEF, and CO (Figure 4B–D; Table S5), indicating compromised left ventricular systolic performance. WGA staining revealed hypertrophic cardiomyocytes with thickened myofibers and enlarged cell boundaries in the 2PY group, and quantitative analysis confirmed a significantly larger CSA compared with the Control group (Figure 4E). Furthermore, plasma ELISA analysis confirmed that circulating stress markers NT-proANP and NT-proBNP were markedly elevated in the 2PY group (Figure 4F,G). In addition, plasma Cr and BUN levels were significantly increased in the 2PY group compared with the Control group (Figure S2), indicating impaired renal function under chronic 2PY exposure. These findings indicate that chronic administration of 2PY was accompanied by impaired cardiac systolic function and hypertrophy-associated myocardial changes in rats under the experimental conditions used in this study.

To elucidate the signaling mechanisms underlying 2PY-induced cardiac injury, the cardiac MEK/ERK cascade was examined. RT-qPCR analysis showed that the mRNA levels of *Map2k1*, *Map2k2*, *Erk1*, and *Erk2* were significantly increased in the 2PY group whereas the transcription levels of *Raf1* remained comparable to that of the Control group (Figure 4H). Western blot analysis further revealed that the phosphorylation levels of MEK and ERK were significantly increased in 2PY-treated hearts, as evidenced by elevated p-MEK/MEK and p-ERK/ERK ratios (Figure 4I and Figure S3). These data indicate that chronic 2PY exposure activates the MEK/ERK signaling pathway at both the transcriptional and post-translational levels, which may contribute to the observed myocardial hypertrophy and systolic dysfunction.

3.5. 2PY Exposure Is Associated with Hypertrophy-Related Changes and MEK/ERK Activation in H9c2 Cells

To characterize the direct cellular effects of 2PY on cardiomyocytes, 1 mM 2PY was selected based on CCK-8 assay results (Figure S4). Phalloidin staining revealed that 2PY treatment increased cell size and induced disorganized actin myofilaments, whereas co-treatment with U0126 significantly attenuated these cytoskeletal abnormalities and partially restored regular cell morphology (Figure 5A). Quantitative analysis confirmed that 2PY significantly increased the cell spread area and this effect was largely abolished by U0126 (Figure 5B). Consistent with these morphological changes, qPCR analysis showed that 2PY significantly increased the mRNA levels of the hypertrophic markers *Nppa*, *Nppb*, and *MYH7*, whereas co-treatment with U0126 significantly attenuated these increases; the U0126-only group did not show induction of these markers (Figure S5). Western blot analysis further demonstrated that 2PY markedly elevated the phosphorylation levels of MEK and ERK without altering their total protein expression (Figure 5C–G and Figure S3). Importantly,

pharmacological inhibition with U0126 effectively blocked 2PY-induced MEK and ERK hyperphosphorylation. These findings support the involvement of MEK/ERK signaling in 2PY-associated hypertrophy-related responses in H9c2 cardiomyocytes.

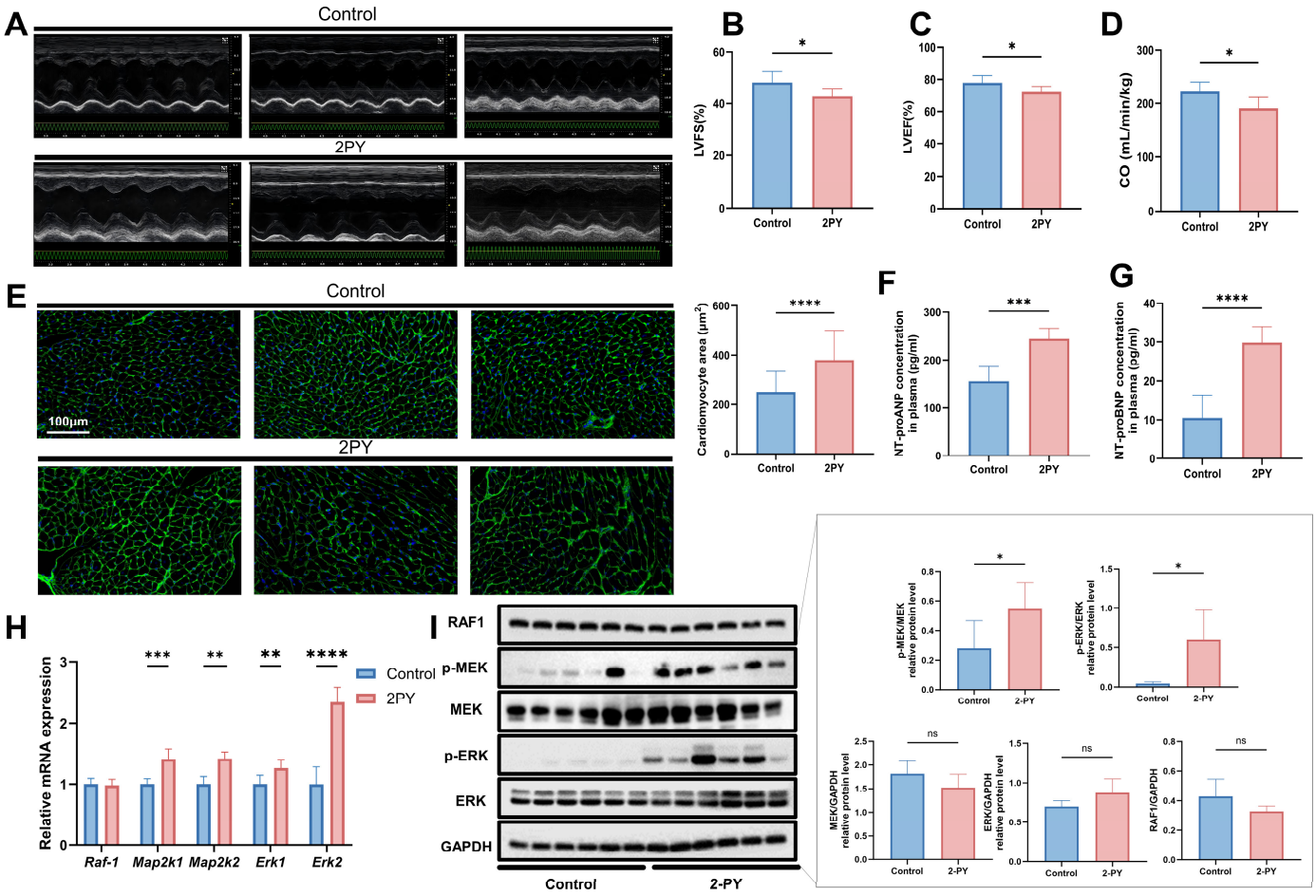

Figure 4. Chronic 2PY exposure impairs cardiac systolic function and induces myocardial hypertrophy with MEK/ERK activation in rats. (**A**) Representative echocardiographic tracings from Control and 2PY-treated rats ($n = 6$). (**B**–**D**) Quantitative analysis of LVFS, LVEF and CO based on echocardiography ($n = 6$). (**E**) Representative immunofluorescence images of rat heart sections stained with WGA-FITC (green, cell membrane) and DAPI (blue, nuclei). Scale bar, 100 μm ($n = 6$). (**F**,**G**) Plasma concentrations of NT-proBNP and NT-proANP measured by ELISA ($n = 6$). (**H**) qRT-PCR detection of relative mRNA levels of *Raf-1*, *Map2k1*, *Map2k2*, *Erk1* and *Erk2* in myocardial tissues ($n = 6$). (**I**) Western blot analysis of RAF1, p-MEK, MEK, p-ERK, ERK and GAPDH ($n = 6$). Data are presented as mean ± SD. * $p < 0.05$, ** $p < 0.01$, *** $p < 0.001$, **** $p < 0.0001$; ns indicates no significant difference.

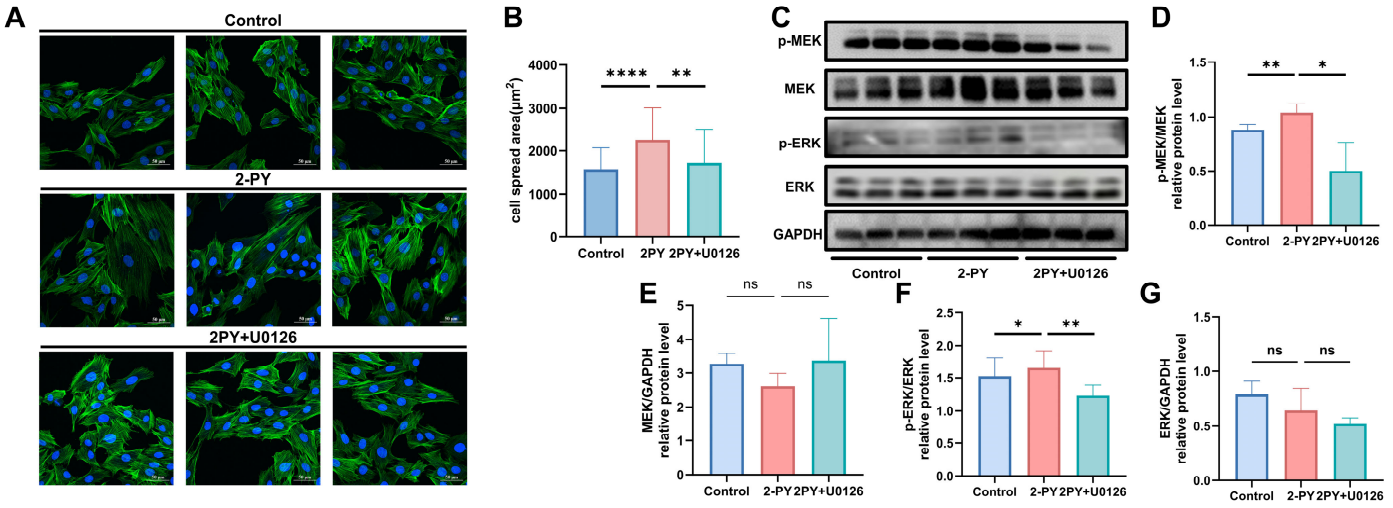

Figure 5. 2PY induces cardiomyocyte hypertrophy through MEK/ERK activation in H9c2 cells. (**A**) Representative immunofluorescence images of H9c2 cells stained with Phalloidin-FITC (green, F-actin) and DAPI (blue, nuclei). Scale bar, 50 μm ($n = 3$). (**B**) Quantitative analysis of projected cell area across the three groups ($n = 3$). (**C**) Western blot detection of p-MEK, total MEK, p-ERK, total ERK and GAPDH protein levels ($n = 3$). (**D**) Quantitative analysis of relative p-MEK/MEK protein abundance ($n = 3$). (**E**) Quantitative analysis of relative MEK/GAPDH protein abundance ($n = 3$). (**F**) Quantitative analysis of relative p-ERK/ERK protein abundance ($n = 3$). (**G**) Quantitative analysis of relative ERK/GAPDH protein abundance ($n = 3$). Data are presented as mean ± SD. * $p < 0.05$, ** $p < 0.01$, **** $p < 0.0001$; ns indicates no significant difference.

3.6. Molecular Docking and Molecular Dynamics Simulation Identify PRKCE as a Candidate Direct Target of 2PY

To identify the potential molecular targets of 2PY, hub proteins were prioritized by integrating the four topological metrics yielding six core hub proteins: PRKCE, MAPK1, HRAS, MAPK10, PTPN11, and PIK3R1 (Figure 6A, Table S6). Among these candidates, PRKCE exhibited the most favorable predicted binding energy with 2PY (Figure 6B, Table S7). Docking analysis further suggested a potential interaction between 2PY and the C1B domain of PRKCE, involving two hydrogen bonds (Figure 6C). MD simulations showed that the 2PY-PRKCE complex reached equilibrium at approximately 10 ns, with RMSD stabilizing at 0.2–0.4 nm, and RMSF analysis demonstrated low fluctuations for residues 248–290 within the core structural domain (Figure 6D,E). The Rg and SASA fluctuated little throughout the simulation (Figure 6F,H), and one or more hydrogen bonds were maintained between 2PY and PRKCE (Figure 6G). MM-PBSA analysis estimated the binding free energy of the simulated 2PY–PRKCE complex to be −42.913 kJ/mol (−10.257 kcal/mol), while Gibbs free energy landscape (GEL) analysis characterized the conformational states sampled during the simulation (Figure 6I). Previous studies have shown that PKCε (encoded by PRKCE) can regulate the MEK/ERK cascade and participate in pathological cardiac remodeling [33,34]. Collectively, these computational findings identify PRKCE as a predicted candidate target of 2PY and suggest a potential interaction between 2PY and PRKCE. Given the reported involvement of PKCε in MEK/ERK signaling, PRKCE may represent a candidate upstream molecule linking 2PY exposure to this pathway; however, direct binding and functional involvement of PRKCE remain to be experimentally validated.

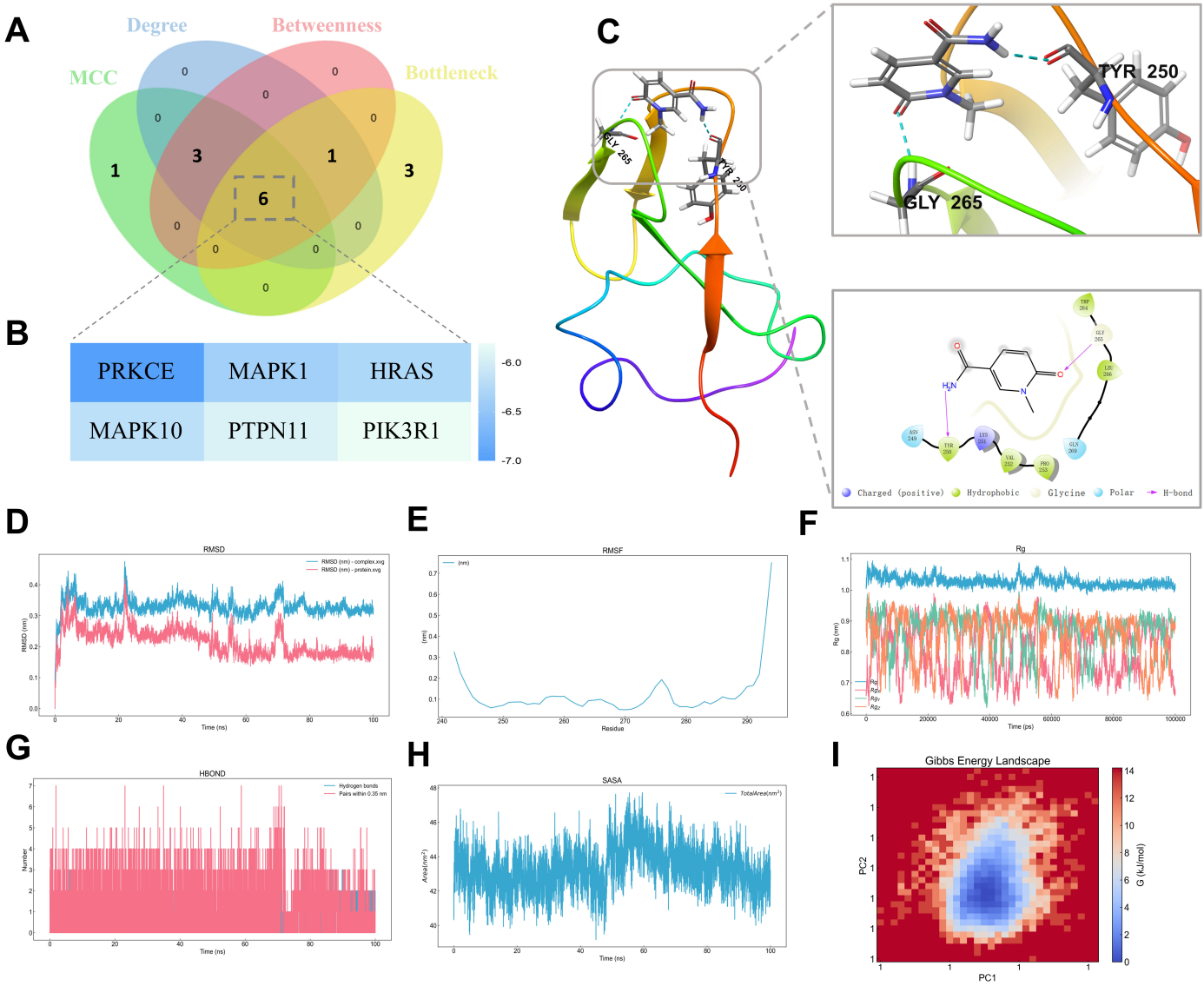

Figure 6. Molecular docking and molecular dynamics analyses of the 2PY-PRKCE complex. (**A**) Venn diagram illustrating overlaps among top-ranked nodes screened by four cytoHubba metrics (MCC, Degree, Betweenness, Bottleneck). Numbers represent the count of shared candidate nodes. (**B**) Heatmap of molecular docking scores for key targets. (**C**) Interaction diagram of the 2PY-PRKCE complex. (**D**) Comparative RMSD analysis of the PRKCE protein and 2PY-PRKCE complex. (**E**) RMSF analysis of the 2PY-PRKCE complex. (**F**) Rg analysis of the 2PY-PRKCE complex. (**G**) Hydrogen bond analysis between 2PY and PRKCE. (**H**) SASA analysis of the 2PY-PRKCE complex. (**I**) 2D gibbs energy landscape of the 2PY-PRKCE complex.

4. Discussion

Cross-organ injury induced by chronic diseases represents a major research focus and persistent challenge in modern medicine [35]. The clinical burden of CRS-4 has been widely recognized by the academic community [36]. Yet its core pathogenic mechanisms remain elusive and specific therapeutic targets have yet to be identified. Studies investigating cardiovascular toxicity in CRS-4 have mainly focused on PBUTs, as they are poorly eliminated by conventional hemodialysis [9,37]. Despite the close association between PBUTs and cardiovascular injury in dialysis populations, existing dialysis strategies have not significantly reduced all-cause mortality [38]. The present study indicates that pathological effects of

small-molecule water-soluble uremic toxins have long been underestimated and may serve as important potential contributors to CRS-4 associated cardiac injury.

2PY is the terminal metabolite of nicotinamide adenine dinucleotide (NAD^+), which is normally excreted in urine under physiological conditions [39]. With the progression of CKD, patients exhibit markedly elevated relative abundance of a plasma metabolomic feature annotated as 2PY that can reach 5-6-fold the levels seen in healthy subjects [23]. Spearman's correlation analysis showed that plasma 2PY concentration was significantly correlated with both LVEF ($\rho = -0.88$, $p < 0.001$) and LVFS ($\rho = -0.78$, $p < 0.01$) in the pooled analysis (Figure 2I). Of particular relevance, a recent landmark clinical study linked circulating 2PY to major adverse cardiovascular events (MACEs) in clinical cohorts [24]. However, we must carefully interpret this association in light of their mechanistic findings, which demonstrated that physiological concentrations of 4-pyridone-3-carboxamide (4PY), a structural isomer, rather than 2PY, drove vascular cell adhesion molecule-1 (VCAM-1) upregulation and leukocyte adhesion in mice. This critical discrepancy highlights the need to separate epidemiological correlation from validated bioactivity, and cautions against directly attributing the vascular pro-inflammatory actions of 4PY to 2PY. Consequently, the specific myocardial effects of 2PY remain largely undefined. Our study addresses this knowledge gap by interrogating the direct cardiac consequences of chronic 2PY exposure in the setting of CRS-4, without asserting 2PY as a general or sole causal mediator of cardiovascular disease. Of note, myo-inositol also exhibited significant correlations with all four echocardiographic parameters. However, the pathogenic role of the myo-inositol and sodium-myo-inositol cotransporter-1 (SMIT1) axis in adverse cardiac remodeling has been well characterized. Circulating myo-inositol is elevated in heart failure, predicts adverse outcomes, and promotes cardiac fibroblast activation in vitro, and genetic deletion of its transporter SMIT1 protects mice against pressure-overload-induced hypertrophy and fibrosis [40,41]. We therefore focused on 2PY, a previously unrecognized metabolite, in subsequent mechanistic investigations. Although we failed to achieve significant enrichment of the nicotinate/nicotinamide metabolism pathway in our plasma metabolomic dataset, this limitation does not negate the biological relevance of 2PY accumulation. As the breakdown product of NAD^+, 2PY reflects the status of cellular redox homeostasis, since NAD^+ serves as an obligate redox cofactor in the TCA cycle and oxidative phosphorylation [42,43]. Consistent with this, the marked enrichment of central carbon metabolism and arginine/amino acid biosynthesis points to a co-perturbation of bioenergetic and nitrogen metabolic programs alongside elevated 2PY.

To our knowledge, this is the first study to demonstrate that isolated 2PY administration can directly induce myocardial hypertrophy and cardiac dysfunction via both in vivo and in vitro assays. Network toxicological analysis identified PRKCE, MAPK1 (ERK2), and HRAS as hub proteins of the MEK/ERK cascade, and molecular docking together with molecular dynamics simulations prioritized PRKCE as a candidate direct target of 2PY. These findings suggest that 2PY may target the regulatory components of this pathway. Both in vivo and in vitro experiments showed that 2PY markedly elevates the phosphorylation levels of MEK and ERK. The MEK-specific inhibitor U0126 effectively reverses 2PY-triggered hypertrophic phenotypes in H9c2 cardiomyocytes and blocked 2PY-induced MEK/ERK hyperphosphorylation. These observations confirm that the MEK/ERK signaling pathway serves as a key mediator of 2PY-elicited cardiotoxicity. Notably, this pro-hypertrophic effect contrasts with the reported renoprotective actions of 2PY. Yoshimura et al. [39] demonstrated that 2PY inhibited renal fibrosis via Akt inhibition without obvious toxicity. This discrepancy indicates that the biological actions of 2PY are highly context-dependent and tissue-specific, potentially driven by distinct signaling cascades. Previous studies have shown that 2PY suppresses PARP-1 activity [22,44]. We therefore hypothesize that 2PY may

drive cellular signal remodeling via regulation of PARP1/NAD^+ metabolism [45]. Meanwhile, cardiac transcriptomic profiling of CRS-4 model rats revealed marked disturbance of energy-metabolic pathways, including oxidative phosphorylation, TCA cycle, and carbon metabolism. Together, these data suggest a metabolic link between 2PY accumulation and the energy metabolic remodeling of myocardial injury in CRS-4.

Previous studies have demonstrated that NAD^+ levels decrease while 2PY accumulation increases in CKD [22,46]. We further assessed the mRNA levels of two key enzymes, NNMT and AOX1, involved in the 2PY-generating pathway. These findings suggest that elevated hepatic NNMT expression might contribute to increased circulating 2PY, in addition to reduced renal clearance in CRS-4 (Figure S1C). To date, NNMT represents a promising therapeutic target in metabolic diseases [47]. Elevated NNMT expression is linked to NAD^+ depletion and metabolic abnormalities [47,48]. Its small-molecule inhibitor JBSNF-000088 blocks nicotinamide methylation, lowers 1-methylnicotinamide levels, and boosts NAD^+ availability and reserves in animal models [49]. Based on our present findings, we hypothesive that NNMT inhibition could confer dual therapeutic benefits in CRS-4. As the upstream rate-limiting enzyme of the 2PY-generating pathway, NNMT suppression could diminish 1-methylnicotinamide and consequently reduce accumulation of the cardiotoxic metabolite 2PY. Meanwhile, it may mitigate excessive NNMT-driven nicotinamide consumption, preserve myocardial NAD^+ pools, and alleviate energy-metabolic perturbations. These findings suggest a potential strategy for metabolic-targeted intervention in CRS-4. Nicotinamide riboside and nicotinamide mononucleotide, widely used NAD^+ precursors for anti-aging and metabolic-health interventions, have been reported to raise circulating 2PY and 4PY levels upon supplementation [50,51]. Integrating our findings, future clinical studies are warranted to evaluate whether dynamic monitoring of plasma 2PY levels could be beneficial for CKD patients receiving NAD^+-precursor interventions.

Our study supports plasma 2PY concentration as a promising novel early-warning biomarker for myocardial hypertrophy and progressive cardiac dysfunction in patients with CRS-4. Furthermore, our findings implicate the MEK/ERK pathway as a key mediator of 2PY-driven myocardial toxicity, providing experimental support for targeted pharmacological intervention against CRS-4. Multiple MEK inhibitors such as trametinib and selumetinib are already used in clinical oncology [52]. Nevertheless, their cardioprotective efficacy and safety have not been systematically assessed in CRS-4 animal models. Moreover, MEK inhibitors may themselves induce cardiac adverse events including left-ventricular dysfunction [53,54], which presents substantial obstacles to clinical translation of this therapeutic strategy.

This work has several limitations that warrant further investigation. First, the actual systemic exposure to 2PY in the intervention experiments remains unknown. Although the nominal target dose was estimated to be 150 mg/kg/day based on assumed body weight and water intake, individual water consumption was not monitored, and neither plasma nor cardiac tissue 2PY concentrations were directly measured. Therefore, we cannot determine whether the achieved systemic exposure corresponded to the concentrations reported in patients with uremia. Furthermore, the 1 mM concentration used in H9c2 cells substantially exceeded reported mean plasma concentrations in patients with uremia, limiting the direct clinical extrapolation of the in vitro findings. Notably, plasma creatinine and BUN levels were also elevated in the 2PY-treated rats, suggesting that changes in renal function or other systemic effects may have contributed to the observed cardiac alterations. Future studies incorporating individual intake monitoring and targeted quantification of 2PY in plasma and cardiac tissue are needed to establish the actual exposure levels and clarify the relationship between 2PY exposure and cardiac remodeling. Second, molecular docking and MD simulations identified PRKCE as a candidate direct target of 2PY, but this result

is computationally predicted. Further experimental validation, such as surface plasmon resonance (SPR) or isothermal titration calorimetry (ITC) binding assays, site-directed mutagenesis of the predicted binding pocket, and PRKCE knockdown/overexpression studies, would be valuable to confirm the direct binding and its functional relevance. Third, blood pressure and RAAS activity were not monitored in either the 5/6 nephrectomy cohort or the separate 2PY intervention cohort. Previous comparative studies have shown that 5/6 nephrectomy models generally exhibit less pronounced early hypertension and RAAS activation, a smaller increase in glomerular capillary pressure, and less severe glomerular injury than infarction-based models [55–58]. However, these findings cannot be directly extrapolated to our experimental animals. Therefore, potential hemodynamic contributions to the observed cardiac phenotypes in both experimental cohorts cannot be excluded. Given that pressure and volume overload are recognized contributors to left ventricular hypertrophy in CKD [59,60], the cardiac alterations observed in this study should not be attributed exclusively to 2PY accumulation or its direct myocardial effects. Future studies incorporating blood pressure monitoring and assessment of RAAS activity are warranted to further clarify the contribution of hemodynamic factors to cardiac remodeling in CRS-4.

5. Conclusions

In conclusion, this study investigated the small-molecule uremic toxin 2PY in the context of myocardial hypertrophy in CRS-4. Our findings demonstrate that 2PY exposure was associated with MEK/ERK activation through concurrent transcriptional upregulation of *Map2k1/2* and *Erk1/2* and enhanced post-translational phosphorylation of MEK and ERK proteins. Pharmacological blockade of MEK by U0126 reversed 2PY-induced cardiomyocyte hypertrophy, supporting a causal role of this signaling axis under our experimental conditions. While network toxicology and computational simulations prioritized PRKCE as a candidate upstream target, its direct involvement requires further experimental validation. Collectively, these results provide experimental evidence that 2PY accumulation is associated with cardiac remodeling in CRS-4. MEK/ERK activation represents a key signalling event linked to 2PY action, and further in vivo intervention studies are required to determine whether this pathway directly mediates 2PY's cardiac effects. These data support its potential utility in cardiovascular risk assessment and highlight MEK/ERK as a candidate target for therapeutic intervention in chronic kidney disease.

Supplementary Materials: The following supporting information can be downloaded at https://www.mdpi.com/article/10.3390/biom16121739/s1, Figure S1: Within-group correlations between Nudifloramide (2PY) and LVEF, and relative hepatic mRNA levels of Nnmt and Aox1; Figure S2: Effects of 2PY exposure on plasma Cr and BUN levels in rats; Figure S3: Uncropped and cropped original Western blot images for Figures 4I and 5C; Figure S4: Effects of 2PY on the viability of H9c2 rat cardiomyocytes; Figure S5: Effects of 2PY and the MEK inhibitor U0126 on the expression of hypertrophic marker genes in H9c2 cells; Figure S6: Conformational dynamics and residue-level flexibility across three independent 100-ns simulations; Table S1: Chromatographic conditions for untargeted plasma metabolomics detection; Table S2: Primer information for analyzed genes; Table S3: Echocardiographic parameters in Sham and Model groups; Table S4: Relative abundance of 182 differential metabolites detected in Sham and model groups; Table S5: Echocardiographic parameters in Control and 2PY groups; Table S6: Topological metrics of candidate hub proteins obtained via cytoHubba analysis; Table S7: The GlideScore of the 2PY and the targets; Table S8: Mean and standard deviation (SD) of RMSD and RMSF.

Author Contributions: Conceptualization, M.W., F.Z. and M.L.; methodology, M.W., Y.L., J.W. and J.F.; software, M.W. and Y.L.; validation, M.W., Y.L., J.W., J.F. and X.D.; formal analysis, M.W. and Y.L.; investigation, M.W., Y.L., J.W., J.F., X.D. and C.J.; resources, C.J., F.Z. and M.L.; data curation, M.W. and Y.L.; writing—original draft preparation, M.W.; writing—review and editing, F.Z. and

M.L.; visualization, M.W. and Y.L.; supervision, F.Z. and M.L.; project administration, M.L.; funding acquisition, F.Z. and M.L. All authors have read and agreed to the published version of the manuscript.

Funding: This research was funded by the Natural Science Foundation of Guangdong Province (No. 2023A1515011814) and the National Natural Science Foundation of China (No. 82374138).

Institutional Review Board Statement: All animal experiments were performed in accordance with the ARRIVE guidelines. The protocol was approved by the Ethics Committee of Southern Medical University (Ethical Approval: SMUL202411005, Approval Date: 9 December 2024).

Informed Consent Statement: Not applicable.

Data Availability Statement: The raw RNA-sequencing data are deposited in the Genome Sequence Archive (GSA) of National Genomics Data Center (NGDC) under accession CRA049101 (https://ngdc.cncb.ac.cn/gsa; accessed on 27 August 2026). All other supporting data are available within the article.

Acknowledgments: The authors thank the laboratory members for their technical support and helpful discussions during this study.

Conflicts of Interest: The authors declare no conflicts of interest.

Abbreviations

The following abbreviations are used in this manuscript:

1-MNA	1-methylnicotinamide
2PY	Nudifloramide
5/6 Nx	5/6 nephrectomy
ANP	Atrial natriuretic peptide
AOX1	Aldehyde oxidase 1
BNP	Brain natriuretic peptide
BP	Biological process
BUN	Blood urea nitrogen
CC	Cellular component
CKD	Chronic kidney disease
Cr	Creatinine
CRS-4	Cardiorenal syndrome type 4
CSA	Cross-sectional area
CCK-8	Cell Counting Kit-8
DAPI	4′,6-diamidino-2-phenylindole
DEGs	Differentially expressed genes
ELISA	Enzyme-linked immunosorbent assay
ERK	Extracellular signal-regulated kinase
EUTox	European Uremic Toxin Work Group
F-actin	Filamentous actin
FBS	Fetal bovine serum
FPKM	Fragments per kilobase of transcript per million mapped reads
GAPDH	Glyceraldehyde-3-phosphate dehydrogenase
GO	Gene Ontology
HRAS	Harvey rat sarcoma viral oncogene homolog
HRP	Horseradish peroxidase
KEGG	Kyoto Encyclopedia of Genes and Genomes
LVEF	Left ventricular ejection fraction
LVFS	Left ventricular fractional shortening
LVIDs	Left ventricular internal diameter in systole
MAPK	Mitogen-activated protein kinase
MEK	Mitogen-activated protein kinase kinase
MF	Molecular function
NAD^+	Nicotinamide adenine dinucleotide
NMN	Nicotinamide mononucleotide
NNMT	Nicotinamide N-methyltransferase
NT-proANP	N-terminal pro-atrial natriuretic peptide

NT-proBNP	N-terminal pro-B-type natriuretic peptide
PARP-1	Poly(ADP-ribose) polymerase 1
PBUTs	Protein-bound uremic toxins
PCA	Principal component analysis
PPI	Protein–protein interaction
PVDF	Polyvinylidene fluoride
RAAS	Renin–angiotensin–aldosterone system
RAF1	RAF proto-oncogene serine/threonine-protein kinase
RIPA	Radioimmunoprecipitation assay
RT-qPCR	Real-time quantitative polymerase chain reaction
SD	Sprague-Dawley
SGLT2	Sodium–glucose cotransporter 2
SIRT1	Sirtuin 1
SDS-PAGE	Sodium dodecyl sulfate-polyacrylamide gel electrophoresis
TBST	Tris-buffered saline with Tween-20
TMAO	Trimethylamine N-oxide
WGA	Wheat germ agglutinin

References

1. Ronco, C.; McCullough, P.; Anker, S.D.; Anand, I.; Aspromonte, N.; Bagshaw, S.M.; Bellomo, R.; Berl, T.; Bobek, I.; Cruz, D.N.; et al. Cardio-renal syndromes: Report from the consensus conference of the acute dialysis quality initiative. *Eur. Heart J.* **2010**, *31*, 703–711. [CrossRef] [PubMed]
2. Mark, P.B.; Stafford, L.K.; Grams, M.E.; Aalruz, H.; Abd ElHafeez, S.; Abdelgalil, A.A.; Abdulkader, R.S.; Abeywickrama, H.M.; Abiodun, O.O.; Abramov, D.; et al. Global, regional, and national burden of chronic kidney disease in adults, 1990–2023, and its attributable risk factors: A systematic analysis for the Global Burden of Disease Study 2023. *Lancet* **2025**, *406*, 2461–2482. [CrossRef] [PubMed]
3. Kobo, O.; Abramov, D.; Davies, S.; Ahmed, S.B.; Sun, L.Y.; Mieres, J.H.; Parwani, P.; Siudak, Z.; Van Spall, H.G.C.; Mamas, M.A. CKD-Associated Cardiovascular Mortality in the United States: Temporal Trends From 1999 to 2020. *Kidney Med.* **2023**, *5*, 100597. [CrossRef] [PubMed]
4. Johansen, K.L.; Gilbertson, D.T.; Li, S.; Li, S.; Liu, J.; Roetker, N.S.; Ku, E.; Schulman, I.H.; Greer, R.C.; Chan, K.; et al. US Renal Data System 2023 Annual Data Report: Epidemiology of Kidney Disease in the United States. *Am. J. Kidney Dis.* **2024**, *83*, A8–A13. [CrossRef] [PubMed]
5. Baaten, C.; Vondenhoff, S.; Noels, H. Endothelial Cell Dysfunction and Increased Cardiovascular Risk in Patients With Chronic Kidney Disease. *Circ. Res.* **2023**, *132*, 970–992. [CrossRef] [PubMed]
6. Wang, X.; Shapiro, J.I. Evolving concepts in the pathogenesis of uraemic cardiomyopathy. *Nat. Rev. Nephrol.* **2019**, *15*, 159–175. [CrossRef] [PubMed]
7. Zhu, Y.; Lv, C.; Yang, H.; Lu, Q.; Wang, X.; Zhang, Y.; Guo, M.; Yang, B. Chronic cardiorenal syndrome: Cardio-renal protective effect of SGLT2i. *Ren. Fail* **2025**, *47*, 2575921. [CrossRef] [PubMed]
8. Verma, D.; Firoz, A.; Garlapati, S.K.P.; Sai, C.R.S.T.; Haris, M.; Dhungana, B.; Ray, B.; Shah, G.; Kc, B.; Paudel, P. Emerging Treatments of Cardiorenal Syndrome: An Update on Pathophysiology and Management. *Cureus* **2021**, *13*, e17240. [CrossRef] [PubMed]
9. Lim, Y.J.; Sidor, N.A.; Tonial, N.C.; Che, A.; Urquhart, B.L. Uremic Toxins in the Progression of Chronic Kidney Disease and Cardiovascular Disease: Mechanisms and Therapeutic Targets. *Toxins* **2021**, *13*, 142. [CrossRef] [PubMed]
10. Long, E.; Heihre, J.M. Recharging the Powerhouse: Mitochondrial Dysfunction and Therapy in Cardiorenal Syndrome Type 4. *Curr. Heart Fail Rep.* **2025**, *22*, 24. [CrossRef] [PubMed]
11. Zhang, Y.; Han, X.; Feng, T.; Li, Z.; Yu, H.; Chen, Y.; Gao, Y.; Gao, Q.; Zhang, L.; Li, S.; et al. Gut-microbiota-derived indole sulfate promotes heart failure in chronic kidney disease. *Cell Host Microbe* **2025**, *33*, 1715–1730. [CrossRef] [PubMed]
12. Lei, D.; Liu, Y.; Liu, Y.; Jiang, Y.; Lei, Y.; Zhao, F.; Li, W.; Ouyang, Z.; Chen, L.; Tang, S.; et al. The gut microbiota metabolite trimethylamine N-oxide promotes cardiac hypertrophy by activating the autophagic degradation of SERCA2a. *Commun. Biol.* **2025**, *8*, 596. [CrossRef] [PubMed]
13. Gao, H.; Liu, S. Role of uremic toxin indoxyl sulfate in the progression of cardiovascular disease. *Life Sci.* **2017**, *185*, 23–29. [CrossRef] [PubMed]
14. Du, Q.; Gao, J.; Lu, R.; Jin, Y.; Zou, Y.; Yu, C.; Yan, Y. Asymmetric dimethylarginine compartmental behavior during high-flux hemodialysis. *Ren. Fail* **2020**, *42*, 760–766. [CrossRef] [PubMed]

15. Xue, Y.; Xu, B.; Su, C.; Han, Q.; Wang, T.; Tang, W. Cardiorenal syndrome in incident peritoneal dialysis patients: What is its effect on patients' outcomes? *PLoS ONE* **2019**, *14*, e0218082. [CrossRef] [PubMed]
16. Flythe, J.E.; Watnick, S. Dialysis for Chronic Kidney Failure: A Review. *Jama* **2024**, *332*, 1559–1573. [CrossRef] [PubMed]
17. Barreto, F.C.; Barreto, D.V.; Liabeuf, S.; Meert, N.; Glorieux, G.; Temmar, M.; Choukroun, G.; Vanholder, R.; Massy, Z.A. Serum indoxyl sulfate is associated with vascular disease and mortality in chronic kidney disease patients. *Clin. J. Am. Soc. Nephrol.* **2009**, *4*, 1551–1558. [CrossRef] [PubMed]
18. Watanabe, H.; Miyamoto, Y.; Enoki, Y.; Ishima, Y.; Kadowaki, D.; Kotani, S.; Nakajima, M.; Tanaka, M.; Matsushita, K.; Mori, Y.; et al. P-Cresyl sulfate, a uremic toxin, causes vascular endothelial and smooth muscle cell damages by inducing oxidative stress. *Pharmacol. Res. Perspect.* **2015**, *3*, e00092. [CrossRef] [PubMed]
19. Ix, J.H.; Shlipak, M.G.; Wassel, C.L.; Whooley, M.A. Fibroblast growth factor-23 and early decrements in kidney function: The Heart and Soul Study. *Nephrol. Dial. Transpl.* **2010**, *25*, 993–997. [CrossRef] [PubMed]
20. Canyelles, M.; Borràs, C.; Rotllan, N.; Tondo, M.; Escolà-Gil, J.C.; Blanco-Vaca, F. Gut Microbiota-Derived TMAO: A Causal Factor Promoting Atherosclerotic Cardiovascular Disease? *Int. J. Mol. Sci.* **2023**, *24*, 1940. [CrossRef] [PubMed]
21. Yu, C.; Zhang, M.; Xia, W. Asymmetric dimethylarginine mediates oxidative stress and atrial remodeling in HL-1 cells. *Front. Med.* **2025**, *12*, 1696845. [CrossRef] [PubMed]
22. Lenglet, A.; Liabeuf, S.; Bodeau, S.; Louvet, L.; Mary, A.; Boullier, A.; Lemaire-Hurtel, A.S.; Jonet, A.; Sonnet, P.; Kamel, S.; et al. N-methyl-2-pyridone-5-carboxamide (2PY)-Major Metabolite of Nicotinamide: An Update on an Old Uremic Toxin. *Toxins* **2016**, *8*, 339. [CrossRef] [PubMed]
23. Duranton, F.; Cohen, G.; De Smet, R.; Rodriguez, M.; Jankowski, J.; Vanholder, R.; Argiles, A. Normal and pathologic concentrations of uremic toxins. *J. Am. Soc. Nephrol.* **2012**, *23*, 1258–1270. [CrossRef] [PubMed]
24. Lim, G.B. Metabolic product of excess niacin is linked to increased risk of cardiovascular events. *Nat. Rev. Cardiol.* **2024**, *21*, 280. [CrossRef] [PubMed]
25. Zhang, Y.; Kompa, A.R. A practical guide to subtotal nephrectomy in the rat with subsequent methodology for assessing renal and cardiac function. *Nephrology* **2014**, *19*, 552–561. [CrossRef] [PubMed]
26. Xianyuan, L.; Wei, Z.; Yaqian, D.; Dan, Z.; Xueli, T.; Zhanglu, D.; Guanyi, L.; Lan, T.; Menghua, L. Anti-renal fibrosis effect of asperulosidic acid via TGF-β1/smad2/smad3 and NF-κB signaling pathways in a rat model of unilateral ureteral obstruction. *Phytomedicine* **2019**, *53*, 274–285. [CrossRef] [PubMed]
27. Zhang, X.; Qu, H.; Yang, T.; Liu, Q.; Zhou, H. Astragaloside IV attenuate MI-induced myocardial fibrosis and cardiac remodeling by inhibiting ROS/caspase-1/GSDMD signaling pathway. *Cell Cycle* **2022**, *21*, 2309–2322. [CrossRef] [PubMed]
28. Zhang, R.; Chen, Y.; Wang, W.; Chen, J.; Liu, D.; Zhang, L.; Xiang, Q.; Zhao, K.; Ma, M.; Yu, X.; et al. Combined transcriptomic and metabolomic analysis revealed that pH changes affected the expression of carbohydrate and ribosome biogenesis-related genes in Aspergillus niger SICU-33. *Front. Microbiol.* **2024**, *15*, 1389268. [CrossRef] [PubMed]
29. Cao, X.; Zhou, X.; Chen, S.; Xu, C. Integration of transcriptomics and metabolomics reveals the responses of the maternal circulation and maternal-fetal interface to LPS-induced preterm birth in mice. *Front. Immunol.* **2023**, *14*, 1213902. [CrossRef] [PubMed]
30. Rosner, M.H.; Reis, T.; Husain-Syed, F.; Vanholder, R.; Hutchison, C.; Stenvinkel, P.; Blankestijn, P.J.; Cozzolino, M.; Juillard, L.; Kashani, K.; et al. Classification of Uremic Toxins and Their Role in Kidney Failure. *Clin. J. Am. Soc. Nephrol.* **2021**, *16*, 1918–1928. [CrossRef] [PubMed]
31. Amador-Martínez, I.; Aparicio-Trejo, O.E.; Aranda-Rivera, A.K.; Bernabe-Yepes, B.; Medina-Campos, O.N.; Tapia, E.; Cortés-González, C.C.; Silva-Palacios, A.; Roldán, F.J.; León-Contreras, J.C.; et al. Effect of N-Acetylcysteine in Mitochondrial Function, Redox Signaling, and Sirtuin 3 Levels in the Heart During Cardiorenal Syndrome Type 4 Development. *Antioxidants* **2025**, *14*, 367. [CrossRef] [PubMed]
32. Dettlaff-Pokora, A.; Swierczynski, J. High Concentrations of Circulating 2PY and 4PY-Potential Risk Factor of Cardiovascular Disease in Patients with Chronic Kidney Disease. *Int. J. Mol. Sci.* **2025**, *26*, 4463. [CrossRef] [PubMed]
33. Xuan, Y.T.; Guo, Y.; Zhu, Y.; Wang, O.L.; Rokosh, G.; Messing, R.O.; Bolli, R. Role of the protein kinase C-epsilon-Raf-1-MEK-1/2-p44/42 MAPK signaling cascade in the activation of signal transducers and activators of transcription 1 and 3 and induction of cyclooxygenase-2 after ischemic preconditioning. *Circulation* **2005**, *112*, 1971–1978. [CrossRef] [PubMed]
34. Takeishi, Y.; Ping, P.; Bolli, R.; Kirkpatrick, D.L.; Hoit, B.D.; Walsh, R.A. Transgenic overexpression of constitutively active protein kinase C epsilon causes concentric cardiac hypertrophy. *Circ. Res.* **2000**, *86*, 1218–1223. [CrossRef] [PubMed]
35. Che, H.; Gao, Y.; Xu, Y.; Xu, H.; Eils, R.; Tian, M. Organ cross-talk: Molecular mechanisms, biological functions, and therapeutic interventions for diseases. *Signal Transduct. Target Ther.* **2026**, *11*, 8. [CrossRef] [PubMed]
36. House, A.A.; Wanner, C.; Sarnak, M.J.; Piña, I.L.; McIntyre, C.W.; Komenda, P.; Kasiske, B.L.; Deswal, A.; deFilippi, C.R.; Cleland, J.G.F.; et al. Heart failure in chronic kidney disease: Conclusions from a Kidney Disease: Improving Global Outcomes (KDIGO) Controversies Conference. *Kidney Int.* **2019**, *95*, 1304–1317. [CrossRef] [PubMed]

37. Zhang, S.; Tang, S.; Liu, Y.; Xue, B.; Xie, Q.; Zhao, L.; Yuan, H. Protein-bound uremic toxins as therapeutic targets for cardiovascular, kidney, and metabolic disorders. *Front. Endocrinol.* **2025**, *16*, 1500336. [CrossRef] [PubMed]
38. Eknoyan, G.; Beck, G.J.; Cheung, A.K.; Daugirdas, J.T.; Greene, T.; Kusek, J.W.; Allon, M.; Bailey, J.; Delmez, J.A.; Depner, T.A.; et al. Effect of dialysis dose and membrane flux in maintenance hemodialysis. *N. Engl. J. Med.* **2002**, *347*, 2010–2019. [CrossRef] [PubMed]
39. Yoshimura, N.; Yamada, K.; Ono, T.; Notoya, M.; Yukioka, H.; Takahashi, R.; Wakino, S.; Kanda, T.; Itoh, H. N-methyl-2-pyridone-5-carboxamide (N-Me-2PY) has potent anti-fibrotic and anti-inflammatory activity in a fibrotic kidney model: Is it an old uremic toxin? *Clin. Exp. Nephrol.* **2023**, *27*, 901–911. [CrossRef] [PubMed]
40. Marino, A.; Cumps, J.; Guilbert, L.; Geiser, A.; Baufays, C.; Ginion, A.; Ferté, L.; Battault, S.; De Matos, F.; Ambroise, J.; et al. Sodium-myo-inositol cotransporter-1, SMIT1, promotes cardiac hypertrophy and fibrosis induced by pressure overload in mice. *Cardiovasc Res.* **2026**, *122*, 578–592. [CrossRef] [PubMed]
41. Pouleur, A.C.; Menghoum, N.; Cumps, J.; Marino, A.; Badii, M.; Lejeune, S.; Legault, J.T.; Boucher, G.; Gruson, D.; Roy, C.; et al. Plasma myo-inositol elevation in heart failure: Clinical implications and prognostic significance. Results from the BElgian and CAnadian MEtabolomics in HFpEF (BECAME-HF) research project. *eBioMedicine* **2024**, *107*, 105264. [CrossRef] [PubMed]
42. Ye, C.; Fu, Y.; Zhou, X.; Zhou, F.; Zhu, X.; Chen, Y. Identification and validation of NAD+ metabolism-related biomarkers in patients with diabetic peripheral neuropathy. *Front. Endocrinol.* **2024**, *15*, 1309917. [CrossRef] [PubMed]
43. Ghanem, M.S.; Caffa, I.; Monacelli, F.; Nencioni, A. Inhibitors of NAD+ Production in Cancer Treatment: State of the Art and Perspectives. *Int. J. Mol. Sci.* **2024**, *25*, 2092. [CrossRef] [PubMed]
44. Rutkowski, B.; Slominska, E.; Szolkiewicz, M.; Smolenski, R.T.; Striley, C.; Rutkowski, P.; Swierczynski, J. N-methyl-2-pyridone-5-carboxamide: A novel uremic toxin? *Kidney Int. Suppl.* **2003**, *63*, S19–S21. [CrossRef] [PubMed]
45. Koczor, C.A.; Saville, K.M.; Andrews, J.F.; Clark, J.; Fang, Q.; Li, J.; Al-Rahahleh, R.Q.; Ibrahim, M.; McClellan, S.; Makarov, M.V.; et al. Temporal dynamics of base excision/single-strand break repair protein complex assembly/disassembly are modulated by the PARP/NAD+/SIRT6 axis. *Cell Rep.* **2021**, *37*, 109917. [CrossRef] [PubMed]
46. Jones, B.A.; Gisch, D.L.; Myakala, K.; Sadiq, A.; Cheng, Y.H.; Taranenko, E.; Panov, J.; Korolowicz, K.; Melo Ferreira, R.; Yang, X.; et al. NAD+ prevents chronic kidney disease by activating renal tubular metabolism. *JCI Insight* **2025**, *10*, e181443. [CrossRef] [PubMed]
47. Sun, W.D.; Zhu, X.J.; Li, J.J.; Mei, Y.Z.; Li, W.S.; Li, J.H. Nicotinamide N-methyltransferase (NNMT): A novel therapeutic target for metabolic syndrome. *Front. Pharmacol.* **2024**, *15*, 1410479. [CrossRef] [PubMed]
48. Jawaria; Zarlashat, Y.; Philippovich, M.; Dósa, E. Nicotinamide N-Methyltransferase in Cardiovascular Diseases: Metabolic Regulator and Emerging Therapeutic Target. *Biomolecules* **2025**, *15*, 1281. [CrossRef] [PubMed]
49. Kannt, A.; Rajagopal, S.; Kadnur, S.V.; Suresh, J.; Bhamidipati, R.K.; Swaminathan, S.; Hallur, M.S.; Kristam, R.; Elvert, R.; Czech, J.; et al. A small molecule inhibitor of Nicotinamide N-methyltransferase for the treatment of metabolic disorders. *Sci. Rep.* **2018**, *8*, 3660. [CrossRef] [PubMed]
50. Alegre, G.F.S.; Pastore, G.M. NAD+ Precursors Nicotinamide Mononucleotide (NMN) and Nicotinamide Riboside (NR): Potential Dietary Contribution to Health. *Curr. Nutr. Rep.* **2023**, *12*, 445–464. [CrossRef] [PubMed]
51. Trammell, S.A.; Schmidt, M.S.; Weidemann, B.J.; Redpath, P.; Jaksch, F.; Dellinger, R.W.; Li, Z.; Abel, E.D.; Migaud, M.E.; Brenner, C. Nicotinamide riboside is uniquely and orally bioavailable in mice and humans. *Nat. Commun.* **2016**, *7*, 12948. [CrossRef] [PubMed]
52. Mincu, R.I.; Mahabadi, A.A.; Michel, L.; Mrotzek, S.M.; Schadendorf, D.; Rassaf, T.; Totzeck, M. Cardiovascular Adverse Events Associated With BRAF and MEK Inhibitors: A Systematic Review and Meta-analysis. *JAMA Netw. Open* **2019**, *2*, e198890. [CrossRef] [PubMed]
53. Benko, J.; Péč, M.J.; Tomčová, Z.; Péčová, M.; Samoš, M. Cardiotoxicity of BRAF/MEK Inhibitors Mimicking Apical Hypertrophic Cardiomyopathy. *Cureus* **2024**, *16*, e72313. [CrossRef] [PubMed]
54. Piscione, M.; Di Marcantonio, M.C.; Pala, B.; Mincione, G. Cancer Therapy-Related Left Ventricular Dysfunction: Are There New Gatekeepers? *BioChem* **2025**, *5*, 25. [CrossRef]
55. Griffin, K.A.; Picken, M.; Bidani, A.K. Method of renal mass reduction is a critical modulator of subsequent hypertension and glomerular injury. *J. Am. Soc. Nephrol.* **1994**, *4*, 2023–2031. [CrossRef] [PubMed]
56. Griffin, K.A.; Picken, M.M.; Churchill, M.; Churchill, P.; Bidani, A.K. Functional and structural correlates of glomerulosclerosis after renal mass reduction in the rat. *J. Am. Soc. Nephrol.* **2000**, *11*, 497–506. [CrossRef] [PubMed]
57. Ibrahim, H.N.; Hostetter, T.H. The renin-aldosterone axis in two models of reduced renal mass in the rat. *J. Am. Soc. Nephrol.* **1998**, *9*, 72–76. [CrossRef] [PubMed]
58. Adam, R.J.; Williams, A.C.; Kriegel, A.J. Comparison of the surgical resection and infarct 5/6 nephrectomy rat models of chronic kidney disease. *Am. J. Physiol. Ren. Physiol.* **2022**, *322*, F639–F654. [CrossRef] [PubMed]

59. Taddei, S.; Nami, R.; Bruno, R.M.; Quatrini, I.; Nuti, R. Hypertension, left ventricular hypertrophy and chronic kidney disease. *Heart Fail Rev.* **2011**, *16*, 615–620. [CrossRef] [PubMed]
60. Kaesler, N.; Babler, A.; Floege, J.; Kramann, R. Cardiac Remodeling in Chronic Kidney Disease. *Toxins* **2020**, *12*, 161. [CrossRef] [PubMed]

Disclaimer/Publisher's Note: The statements, opinions and data contained in all publications are solely those of the individual author(s) and contributor(s) and not of MDPI and/or the editor(s). MDPI and/or the editor(s) disclaim responsibility for any injury to people or property resulting from any ideas, methods, instructions or products referred to in the content.